On negative induced polarization in frequency domain measurements

Chen Wang[1], Andrew Binley[2] and Lee D. Slater[1]

[1] Department of Earth and Environmental Sciences, Rutgers University, Newark, New Jersey, USA

[2] Lancaster Environment Centre, Lancaster University, Lancaster, UK

Abbreviated title: Frequency domain negative IP effects

Corresponding author:

Chen Wang

Phone: +1 973-353-5100; Fax: +1 973-353-1965;

Email: cw701@scarletmail.rutgers.edu

Summary

Induced polarization (IP) has been widely used to non-invasively characterize electrical conduction and polarization in the subsurface resulting from an applied electric field. Earth materials exhibit a lossy capacitance defined by an intrinsic negative phase in frequency-domain IP (FDIP) or positive intrinsic chargeability in time-domain IP (TDIP). However, error-free positive apparent phase or negative apparent chargeability (i.e., negative IP effects) can occur in IP measurements over heterogeneous media. While negative IP effects in TDIP datasets have been discussed, no studies have addressed this topic in detail for FDIP measurements. We describe theory and numerical modeling to explain the origin of negative IP effects in FDIP measurements. A positive apparent phase may occur when a relatively high polarizability feature falls into negative sensitivity zones of complex resistivity measurements. The polarity of the apparent phase is determined by the distribution of subsurface intrinsic phase and resistivity, with the resistivity impacting the apparent phase polarity via its control on the sensitivity distribution. A physical explanation for the occurrence of positive apparent phase data is provided by an electric circuit model representing a four-electrode measurement. We also show that the apparent phase polarity will be frequency dependent when resistivity changes significantly with frequency (i.e. in the presence of significant IP effects). Consequently, negative IP effects manifest themselves in the shape of apparent phase spectra recorded with multi-frequency (spectral IP) datasets. Our results imply that positive apparent phase measurements should be anticipated and should be retained during inversion and interpretation of single frequency and spectral IP datasets.

Key words: Electrical properties; Hydrogeophysics; Electromagnetic theory

1. Introduction

Induced polarization (IP), a non-invasive electrical geophysical technique for subsurface characterization, has been widely used in various fields including hydrogeology, engineering, mining exploration and environmental problems (e.g., Pelton *et al.* 1978; Slater & Lesmes 2002; Flores *et al.* 2012; Saneiyan *et al.* 2019). IP measures both electrical conduction (i.e., resistivity) and polarization in a porous medium, therefore providing additional information beyond the direct current resistivity method. The polarization is quantified by either a chargeability in time-domain IP (TDIP) or a phase in frequency-domain IP (FDIP) measurements (Binley & Kemna 2005). The intrinsic capacitive properties of Earth materials are characterized by a positive intrinsic chargeability (in TDIP) or a negative intrinsic phase when expressed in impedance or complex resistivity space (in FDIP). One would therefore expect a positive apparent (measured) chargeability, or equivalently a negative apparent (measured) phase, which we define here as the normal (or positive) recorded IP response (Ward 1988).

In field data acquisition, a negative IP response, i.e., a negative apparent chargeability or a positive apparent phase, is sometimes observed in the measurements. Such negative IP measurements are often treated as errors and deleted during the data inversion or interpretation (e.g., Mary *et al.* 2016; Ntarlagiannis *et al.* 2016; Kelter *et al.* 2018; Garcia-Artigas *et al.* 2020). While negative IP responses may indeed reflect measurement artifacts, they can also result from the distortion of the electric field for certain types of heterogeneity close to the electrodes. Negative IP effects in TDIP measurements resulting from such effects have been investigated (Nabighian & Elliot 1976; Sumner 1976; Komarov 1980; Dahlin & Loke 2015). Dahlin & Loke (2015) conclude that negative apparent chargeability results when highly polarizable features fall within zones of negative resistivity measurement sensitivity for the utilized electrode configuration. They found that the resistivity distribution influences the occurrence and magnitude of negative apparent chargeability data. Such negative IP measurements provide information about the distribution of features in the subsurface and should not simply be removed during data processing (Binley 2015; Dahlin & Loke 2015).

Negative IP effects in FDIP have seldom been reported and studied. Luo and Zhang (1998) presented analytical solutions that predict a positive apparent phase for a buried polarizable sphere measured by a dipole-dipole array. Some recent complex resistivity imaging studies (Flores Orozco *et al.* 2018; Liu *et al.* 2017) reported positive apparent phase measurements and included them in the inversion per recommendations of Dahlin & Loke (2015) for TDIP datasets. Although frequency and time domain signals are in principle equivalent via the Fourier transform when the frequency/time range is adequately large, the two commonly measured IP parameters, FDIP apparent phase and TDIP apparent chargeability, are not directly equivalent.

The apparent chargeability equation developed by Seigel (1959), extended by V. Komarov and colleagues in Russia shortly after Seigel's publication (Komarov 1960), provides a theoretical explanation for negative IP in TDIP measurements. To the knowledge of the authors, no equivalent formulation to explain the existence of negative IP in FD measurements has been presented. Considering the commonly established approximate proportionality between phase and chargeability (e.g., Van Voorhis *et al.* 1973; Lesmes & Frye 2001), we might expect similarities in the behavior of negative IP in FDIP measurements to that observed in TDIP reported by Dahlin & Loke (2015). However, the significance of negative IP effects in FDIP measurements remains poorly understood, especially with respect to spectral IP where the frequency dependence of IP measurements is recorded. In this study, we integrate theory, numerical modeling, equivalent electric circuits and laboratory measurements to comprehensively investigate negative IP effects in FDIP, including single frequency and spectral IP measurements.

2. Theory of negative IP effects

The intrinsic electrical properties of the subsurface are described by a complex resistivity (ρ^*) or its inverse, the complex conductivity (σ^*):

$$\rho^* = |\rho^*|e^{i\varphi} = \frac{1}{\sigma^*}, \tag{1}$$

where $|\rho^*|$ is the complex resistivity magnitude, φ is the complex resistivity phase ($\varphi \leq 0$) and i is the imaginary unit with $i^2 = -1$. Both ρ^* and σ^* can also be presented in terms of real and imaginary components that are directly related to the physical (e.g., pore geometry) and chemical properties of the subsurface.

Field scale FDIP data are most commonly acquired using a four-electrode arrangement at the Earth surface. Two electrodes inject a known sinusoidal alternating electrical current ($\tilde{I}_0$) at various frequencies, while the other two electrodes record the resultant sinusoidal voltage (or potential difference, $\Delta\tilde{U}$). According to Ohm's Law, the measured impedance Z^*_{app} (with magnitude $|Z^*_{\mathrm{app}}|$ and φ_{app}) is determined as,

$$Z^*_{\mathrm{app}} = \left|Z^*_{\mathrm{app}}\right|e^{i\varphi_{\mathrm{app}}} = \frac{\Delta\tilde{U}}{\tilde{I}_0} = \frac{\left|\Delta\tilde{U}\right|\sin(\omega t + \varphi_{\Delta\mathrm{U}})}{\left|\tilde{I}_0\right|\sin(\omega t)} = \frac{\left|\Delta\tilde{U}\right|}{\left|\tilde{I}_0\right|}e^{i\varphi_{\Delta\mathrm{U}}}, \tag{2}$$

where ω is the angular frequency, t is time, $|\tilde{I}_0|$ is the current amplitude, $|\Delta\tilde{U}|$ is the voltage amplitude and $\varphi_{\Delta\mathrm{U}}$ is the phase shift of the voltage sinusoid relative to the current sinusoid $\tilde{I}_0$

(defined as the zero phase reference). The apparent complex resistivity ρ^*_{app} (with magnitude $|\rho^*_{\mathrm{app}}|$ and the same phase φ_{app} as that of Z^*_{app}) is determined using the geometric factor of the applied electrode array K,

$$\rho^*_{\mathrm{app}} = \left|\rho^*_{\mathrm{app}}\right| e^{i\varphi_{\mathrm{app}}} = K Z^*_{\mathrm{app}} = K\left|Z^*_{\mathrm{app}}\right| e^{i\varphi_{\mathrm{app}}}. \tag{3}$$

ρ^*_{app} is the complex resistivity of a homogeneous space equivalent to the value of Z^*_{app} resulting from application of Eq. (3). Eqs. (2) and (3) show that ρ^*_{app}, Z^*_{app}, and $\Delta\tilde{U}$ are linearly related parameters with differing magnitude but the same phase value.

For a heterogeneous subsurface with a two-dimensional distribution of intrinsic complex resistivity ρ^* (i.e., ρ^* varies in horizontal x and vertical z but constant in y direction), the potential U at coordinate (x, y, z) due to a point current source I is described by the Fourier transformed Poisson's equation (e.g., Kemna 2000; Binley 2015),

$$\frac{\partial}{\partial x}\left(\frac{1}{\rho^*}\frac{\partial v^*}{\partial x}\right) + \frac{\partial}{\partial z}\left(\frac{1}{\rho^*}\frac{\partial v^*}{\partial z}\right) - \frac{v^* k^2}{\rho^*} = -I\delta(x)\delta(z), \tag{4}$$

$$U(x, y, z) = \frac{1}{\pi}\int_0^\infty v^*(x, k, z)\cos(ky)\, dk\,, \tag{5}$$

where δ is the Dirac delta function, v^* is the Fourier transformed complex voltage and k is the wave number. Eqs. (4) and (5) are solved numerically via discretization, for example using the finite element method. The superposition of calculated potentials at the potential (voltage recording) electrodes and application of Eqs. (2) and (3) yields the ρ^*_{app} of four-electrode measurements acquired over a heterogeneous ρ^* subsurface.

To investigate the occurrence of negative IP in FDIP (i.e., a positive φ_{app}), we consider a subsurface modeled by a number of small cells with each cell j (j = 1, 2, …, M) characterized by an intrinsic complex resistivity ρ_{j}^{*} (with magnitude $|\rho_{\mathrm{j}}^{*}|$ and phase φ_{j}). If we consider cells parameterized in terms of the logarithms, $\ln \rho_{\mathrm{j}}^{*}$, and measurements equivalently expressed as $\ln \rho_{\mathrm{app}}^{*}$, then for a single four-electrode measurement, the sensitivity to the cell j (S_{j}^{*}) quantifies how the change in $\ln \rho_{\mathrm{j}}^{*}$ changes $\ln \rho_{\mathrm{app}}^{*}$,

$$S_{\mathrm{j}}^{*} = \frac{\partial \ln \rho_{\mathrm{app}}^{*}}{\partial \ln \rho_{\mathrm{j}}^{*}} = \frac{\partial \ln\left(\left|\rho_{\mathrm{app}}^{*}\right| e^{\varphi_{\mathrm{app}} i}\right)}{\partial \ln\left(\left|\rho_{\mathrm{j}}^{*}\right| e^{\varphi_{\mathrm{j}} i}\right)} = \frac{\partial\left(\ln\left|\rho_{\mathrm{app}}^{*}\right| + \varphi_{\mathrm{app}} i\right)}{\partial\left(\ln\left|\rho_{\mathrm{j}}^{*}\right| + \varphi_{\mathrm{j}} i\right)} \tag{6}$$

Different from a conventional direct current (DC) resistivity measurement, S_{j}^{*} of the FDIP measurement is a complex number. As the derivatives of the complex functions in Eq. (6) satisfy the Cauchy-Riemann conditions (Kemna 2000), the following sensitivity components can be expressed as the real part of S_{j}^{*}:

$$S_{\mathrm{j}} = \frac{\partial \ln\left|\rho_{\mathrm{app}}^{*}\right|}{\partial \ln\left|\rho_{\mathrm{j}}^{*}\right|} = \frac{\partial \varphi_{\mathrm{app}}}{\partial \varphi_{\mathrm{j}}}. \tag{7}$$

The imaginary part of S_{j}^{*} is,

$$S_{\mathrm{j,\,im}} = \frac{\partial \ln\left|\rho_{\mathrm{app}}^{*}\right|}{\partial \varphi_{\mathrm{j}}} = -\frac{\partial \varphi_{\mathrm{app}}}{\partial \ln\left|\rho_{\mathrm{j}}^{*}\right|}. \tag{8}$$

Although we mainly focus on the discussion of a single four-electrode measurement, it should be noted that a matrix comprising of S_{j} from a sequence of four-electrode measurements is the Jacobian matrix used, for example, in a gradient-based inverse problem. In Eq. (7), the sensitivity expressed in terms of complex resistivity magnitude is equivalent to that obtained for DC resistivity measurements, which can take either positive or negative values. An increase of $|\rho_j^*|$ in a positive S_j zone will increase $|\rho_{app}^*|$, whereas an increase of $|\rho_j^*|$ in a negative S_j zone will decrease $|\rho_{app}^*|$. An equivalent pattern holds for the phase terms as shown in Eq. (7). To illustrate, assume that the subsurface space has zero phase (i.e., is non-polarizable), and thus $\varphi_{app} = 0$. If the phase of an arbitrary cell φ_j decreases slightly to a negative value (i.e., becomes polarizable), φ_{app} will decrease to be < 0 if this polarizable cell is located in a zone of positive S_j. However, φ_{app} may increase to be > 0 (i.e., negative IP signal) if this polarizable cell is in a zone of negative S_j. This provides a theoretical basis for the presence of positive φ_{app} (negative IP effects) in FDIP measurements, i.e., $\varphi_{app} > 0$ is possible although all $\varphi_j \leq 0$. The imaginary sensitivity (Eq. 8) plays a negligible role as shown later.

While the above arguments are based on the analysis of a single cell φ_j and S_j, a more generalized way is to consider the collective impacts from all the cells. Kemna (2000) exploited the expression in Eq. (7) by forming a "final phase improvement" in the inversion of complex resistivity data once satisfactory matching of the resistivity magnitudes was achieved. Building on this, consider an expression for the inversion of phase angles using the Gauss-Newton approach (neglecting any damping or regularization for simplicity) (e.g., Kemna 2000; Binley 2015),

$$[\boldsymbol{S}^T\boldsymbol{S}]\Delta\boldsymbol{m} = \boldsymbol{S}^T[\boldsymbol{d} - F(\boldsymbol{m}_k)] \tag{9}$$

$$\boldsymbol{m}_{k+1} = \boldsymbol{m}_k + \Delta\boldsymbol{m} \tag{10}$$

where $\boldsymbol{S}$ is the sensitivity matrix for a sequence of four-electrode measurements, $\boldsymbol{d}$ is a vector of measured data (φ_{app} in this case), F is the forward modeling operator, $\boldsymbol{m}$ is a vector of the model parameters (φ_j in this case), $\boldsymbol{m}_k$ and $\boldsymbol{m}_{k+1}$ are the model parameter set at iteration k and k+1, respectively, $\Delta\boldsymbol{m}$ is the model parameter update at iteration k. Assuming that the inversion is achieved with only one step from a starting model with all $\varphi_j = 0$, we have $\boldsymbol{m}_k = \mathbf{0}$, $F(\boldsymbol{m}_k) = \mathbf{0}$, $\boldsymbol{m}_{k+1} = \Delta\boldsymbol{m}$. We can then write Eq. (9) as,

$$\boldsymbol{S}\Delta\boldsymbol{m} = \boldsymbol{d}. \tag{11}$$

In this simplified one-step inversion, $\Delta\boldsymbol{m}$ is essentially the final model that matches $\boldsymbol{d}$. Again, if we only consider a single four-electrode measurement, Eq. (11) gives,

$$\sum_{\mathrm{j}=1}^{M} S_{\mathrm{j}}\, \varphi_{\mathrm{j}} = \varphi_{\mathrm{app}}. \tag{12}$$

This approximation describes the collective impacts of φ_j and S_j from all the cells. Eq. (12) explicitly shows that even when all $\varphi_j \leq 0$ ($j = 1, 2, \ldots, M$), φ_{app} can be positive when relatively more negative φ_j cells concurrently have $S_j < 0$. The polarity of φ_{app} will therefore depend on the relative values of intrinsic phase and the sensitivity, where the latter is affected by the quadrupole geometry and distribution of the intrinsic resistivity.

A similar association between negative IP signals and the sensitivity distribution is recognized in TDIP data (Dahlin & Loke 2015). In TDIP, a unidirectional current is driven between the current electrodes for a period of time and then abruptly switched off. The voltage V_p recorded right before switching off is used to obtain the apparent DC resistivity $\rho_{\mathrm{app}}^{(\mathrm{DC})}$ (assuming the current injection is long enough to approximate a DC condition). After switching off the current, V_p drops suddenly to a secondary voltage V_s, which then decays with time. Seigel (1959) defined the apparent chargeability (m_{app}) as the ratio of V_s to V_p to quantify the TDIP polarization strength.

Considering the same scenario where the subsurface is modeled by M small cells with index j, the theoretical relationship between a single measure of $\rho_{\mathrm{app}}^{(\mathrm{DC})}$ and m_{app}, and the intrinsic parameters $\rho_{\mathrm{j}}^{(\mathrm{DC})}$ and m_{j} making up the subsurface is (Seigel, 1959),

$$m_{\mathrm{app}} = \sum_{\mathrm{j}=1}^{M} \frac{\partial \ln \rho_{\mathrm{app}}^{(\mathrm{DC})}}{\partial \ln \rho_{\mathrm{j}}^{(\mathrm{DC})}} m_{\mathrm{j}} = \sum_{\mathrm{j}=1}^{M} S_{\mathrm{j}}^{(\mathrm{DC})} m_{\mathrm{j}}. \tag{13}$$

where $S_{\mathrm{j}}^{(\mathrm{DC})}$ is the sensitivity to a cell j in terms of DC resistivity, being analogous to the sensitivity in terms of complex resistivity magnitude (Eq. (7)). Eq. (13) has essentially the same structure as Eq. (12). With all $m_{\mathrm{j}} \geq 0$ ($j = 1, 2, \ldots, M$) for Earth materials, the polarity of m_{app} is decided by the polarity of $S_{\mathrm{j}}^{(\mathrm{DC})}$ and the relative values of m_{j}. Eq. (13) predicts that negative m_{app} is possible when features with relatively high m_{j} fall into negative sensitivity zones, providing theoretical support for the negative IP effects in TDIP. In practice, m_{app} defined by Seigel (1959) is difficult to measure and an integral chargeability is instead commonly measured (Binley 2015), which can exhibit equivalent negative IP effects (Dahlin & Loke 2015).

We stress that laboratory measurements of intrinsic complex resistivity or chargeability on a core or soil sample (considered homogeneous at the measurement scale but in fact likely to contain small scale heterogeneity) can never exhibit negative IP effects when 1D current flow is maintained. Such negative IP effects sometimes reported in the literature (e.g., Abdulsamad *et al.* 2016; Saneiyan *et al.* 2018; Bate *et al.* 2020) can only arise from measurement errors.

3. Numerical modeling

To investigate the behavior of the φ_{app} polarity, 2D forward modeling of synthetic intrinsic complex resistivity distributions was performed using cR2 (http://www.es.lancs.ac.uk/people/amb/Freeware/cR2/cR2.htm) in its python wrapper ResIPy (Blanchy *et al.* 2020). The region of interest of the synthetic model contains 25 electrodes spaced 2 m apart for a total length of 48 m and extends to 8 m depth (Figure 1). A quadrilateral mesh with each mesh cell of size 0.25 × 0.25 m (i.e., 8 nodes per electrode) was used for the computations. In this case, each mesh cell corresponds to a small cell *j* described in Section 2. This mesh extends a large distance beyond the region of interest and incorporates boundary conditions that approximate an infinitely large model space. Different intrinsic resistivity and phase values were assigned to different regions to illustrate specific aspects of negative IP effects predicted by theory. Forward models were run to determine φ_{app} of either a single four-electrode measurement or to construct a pseudosection from a sequence of measurements. The four electrodes include a pair of electrodes (positive C+ and negative C-) for current injection and a pair of electrodes (positive P+ and negative P-) for voltage (potential) measurements.

The sensitivity distribution for a single four-electrode measurement on a selected synthetic model was computed using cR2, with a vector of S_j^* corresponding to each mesh cell in the modeling space as the output (Eq. 6). No noise was added to the forward modeling and sensitivity distribution calculation so as to avoid the complicating effects of random errors on the modeling results.

3.1 Influence of sensitivity distribution

The sensitivity distribution for a dipole-dipole array (E10=C+, E12=C-, E14=P-, E16=P+) and also for a Wenner array (E10=C+, E12=P+, E14=P-, E16=C-) was first computed for a homogeneous, low polarizability half-space ($|\rho^*|$ =100 Ω m, φ = –1 mrad) (Figure 2). The imaginary sensitivity (Eq. (8), Figure 2c and 2d) exerts a negligible control on the measurements as its values are many orders of magnitude less than the real sensitivity (Eq. (7), Figure 2a and 2b). A simulation on a homogenous, high polarizability half-space ($|\rho^*|$ =100 Ω m, φ = –100 mrad) results in similar negligible response in the imaginary sensitivity distribution, again being many orders of magnitude less than the real sensitivity. We therefore refer to the real sensitivity in all future discussion of sensitivity patterns. Different patterns of positive and negative sensitivity are observed for the dipole-dipole (Figure 2a) and Wenner arrays (Figure 2b). The sensitivity of zones away from the electrode array is close to zero, therefore having a negligible effect on the ρ^*_{app} measurement.

To illustrate the influence of the sensitivity distribution on the polarity of the measured phase, new forward models were run where φ_{app} of a single measurement using E10, E12, E14 and E16 was computed with a small polarizable cell ($|\rho^*|$ =100 Ω m and φ = –100 mrad) of the same size as a mesh cell (0.25 × 0.25 m) placed at various locations in a background non-polarizing half space ($|\rho^*|$ =100 Ω m, φ = 0 mrad) (Figure 3a). Starting from the first mesh cell, the polarizable cell was moved to the right and down one cell by one cell to cover the horizontal distance from 15 to 24 m and the depth range from 0 to 6 m (containing the zone of enhanced sensitivity). With the polarizable cell at each mesh cell location, the apparent phase φ_{app} of a dipole-dipole array (E10=C+, E12=C-, E14=P-, E16=P+) and a Wenner array (E10=C+, E12=P+, E14=P-, E16=C-)

was computed. Figure 3 shows φ_{app} plotted against the sensitivity of the location with the polarizable cell for the corresponding measurement array. The polarity of φ_{app} is the inverse of the polarity of the sensitivity, i.e., the polarizable cell placed in positive sensitivity zones results in negative φ_{app} and the polarizable cell placed in negative sensitivity zones results in positive φ_{app}. The magnitude of the negative IP signal increases linearly with the magnitude of the negative sensitivity.

3.2 Influence of heterogeneity

We next investigate the effect of heterogeneity on the sensitivity and hence the φ_{app} polarity pattern. A 3 × 3 m polarizable block was located between 22.5 m and 25.5 m along the line and placed at a depth of 0 m to 3 m (Figure 4a). The background was set with $\varphi_{bgk} = -1$ mrad (low polarization) and $|\rho^*_{bgk}| = 100\ \Omega$ m, while the polarizable block was assigned $\varphi_{block} = -100$ mrad and $|\rho^*_{block}|$ equal to either 50, 100 or 200 Ω m. For each $|\rho^*_{block}|$ scenario, a φ_{app} pseudosection was computed for a dipole-dipole array sequence with $a = 4$ m and $n = 1, 2, 3$ and 4 (i.e., electrodes placed in the order C+, C-, P-, P+ with spacing a, $a \times n$ and a between C+ and C-, C- and P-, and P- and P+, respectively) (Figure 4b). The results show that the resistivity of the polarizable block has a significant influence on the polarity and magnitude of φ_{app} within the zones indicated by the dashed triangles. These φ_{app} values increase from negative to positive (i.e. negative IP effect) as $|\rho^*_{block}|$ increases from 50 to 100 Ω m. Higher positive values of φ_{app} (i.e., enhanced negative IP effects) are observed for $|\rho^*_{block}|$ equal to 200 Ω m.

This control of the resistivity of the heterogeneity on the polarity of φ_{app} results from how the presence of the heterogeneity modifies the sensitivity distribution relative to a homogeneous resistivity medium. To illustrate this, a single φ_{app} measurement using E10=C+, E12=C-, E14=P-, E16=P+ (pointed out by arrows in Figure 4b) is used as an example. The corresponding sensitivity distribution for the three synthetic models with different $|\rho^{*}_{\mathrm{block}}|$ values is shown in Figure 4c. As $|\rho^{*}_{\mathrm{block}}|$ increases from 50 to 100, and then to 200 Ω m, φ_{app} increases from –14 mrad to 9 mrad for the 100 Ω m block and to 33 mrad for the 200 Ω m block. This increase of φ_{app} toward more positive values with increasing $|\rho^{*}_{\mathrm{block}}|$ can be explained by the expansion of the negative sensitivity zones within the polarizable block boundary as $|\rho^{*}_{\mathrm{block}}|$ increases (Figure 4c). This change in the sensitivity pattern is highlighted by the difference in sensitivity referenced to the sensitivity for the $|\rho^{*}_{\mathrm{block}}|$ =100 Ω m scenario, where $|\rho^{*}_{\mathrm{block}}|$ = 50 Ω m and $|\rho^{*}_{\mathrm{block}}|$ = 200 Ω m highlights increased and decrease sensitivity respectively within the block boundary (Figure 4d). This confirms that the resistivity heterogeneity has a significant influence on the polarity of φ_{app} by changing the sensitivity distribution.

So far, we have shown that the polarity of φ_{app} is determined by three major factors: (1) the location of polarizable objects relative to positive/negative sensitivity zones; (2) the intrinsic phase of the polarizable objects relative to the surrounding subsurface; (3) the subsurface resistivity heterogeneity that changes the sensitivity patterns. To illustrate the collective impacts of the intrinsic resistivity and intrinsic phase, we computed φ_{app} for a dipole-dipole array (E10=C+, E12=C-, E14=P-, E16=P+) using the same model structure and background settings as shown in Figure 4a, but with $|\rho^{*}_{\mathrm{block}}|$ varying from 20 to 200 Ω m and φ_{block} varying from –5 to –120 mrad

(Figure 5a). When $|\rho^*_{block}|$ =20, 40 or 60 Ω m, all φ_{app} are negative and become more negative with φ_{block} changing from –5 to –120 mrad. When $|\rho^*_{block}|$ =80, 100, 120 or 140 Ω m, φ_{app} is negative when φ_{block} is small (–5 mrad), but becomes positive when φ_{block} is more negative. At $|\rho^*_{block}|$ above 140 Ω m, all φ_{app} are positive even when φ_{block} is only –5 mrad; again, φ_{app} becomes more positive as φ_{block} becomes more negative. A clear transition from negative φ_{app} to positive φ_{app} can be observed in Figure 5a, which shows that a higher $|\rho^*_{block}|$ relative to $|\rho^*_{bgk}|$ tends to result in positive φ_{app}. The φ_{app} pattern will also be affected by other factors, for example the background phase φ_{bgk}. Figure 5b presents the φ_{app} change when φ_{bgk} is set to be –10 mrad. In this situation, more points show negative φ_{app} with positive φ_{app} only occurring when $|\rho^*_{block}|$ is sufficiently large and φ_{block} is sufficiently negative.

The shape of the polarizable block also determines the φ_{app} change under various $|\rho^*_{block}|$ and φ_{block} conditions. Figure 5c shows the simulation with the same model settings as that in Figure 5a except that the vertical extent of the polarizable block is reduced to be between 0 to 1 m. In this case, most of the points show positive φ_{app} due to the increased portions of negative sensitivity zone in the polarizable block. For example, in the case of $|\rho^*_{block}|$ = 100 Ω m in Figure 4c, when the vertical extent of the polarizable block is reduced to be between 0 to 1 m, most of the regions within the block would have negative sensitivity. In this situation, positive φ_{app} is more likely as per Eq. (12).

The above results were obtained from simple, heterogenous synthetic models. For a real subsurface, the interactions between complicated structures and zones may result in various φ_{app} patterns, making it difficult to generalize about what situations will result in negative IP effects.

One important observation from Figure 5 is that even weakly polarizable objects (e.g., $\varphi_{\text{block}} = -5$ and -10 mrad) may produce negative IP signals, especially when the objects have high resistivity relative to the background (e.g., polarizable objects characterized by low water content, low porosity or high electrical resistivity pore fluids).

4. A physical explanation of negative IP effects using an electrical circuit

We have so far explained the occurrence of negative IP signals using theory and numerical modeling. Next, we seek a more physical explanation as a positive phase implies that the electrical current lags the voltage, which is considered to be non-physical in the presence of IP effect. We use a simplified electrical circuit model to provide a physical explanation for negative IP effects. We consider a subsurface represented by a resistor/impedance network circuit (Figure 6a). A sinusoidal current $\tilde{I}_0$ with fixed amplitude $|\tilde{I}_0|$ and zero reference phase is injected between C+ and C-, while the resultant sinusoidal voltage $\Delta\tilde{U}$ (with amplitude $|\Delta\tilde{U}|$ and phase $\varphi_{\Delta U}$) is measured between P+ and P- in the same manner as a dipole-dipole array. Comparing the relative locations of the circuit components in Figure 6a with Figure 2a, Z_1^* (with magnitude $|Z_1^*|$ and phase φ_1) and Z_2^* (with magnitude $|Z_2^*|$ and phase φ_2) represent impedance components located in the positive and negative sensitivity zones, respectively. We next evaluate how changes of Z_1^* or Z_2^* alter the apparent measured impedance Z_{app}^* (i.e., $\Delta\tilde{U}/\tilde{I}_0$).

To make the analysis simple, we set all other circuit components to be pure resistors (represented by symbol 'R'). According to Figure 6a, $\tilde{I}_0$ exits the network via 'C-' by passing Z_1^*, Z_2^*, R_3, R_4 and R_5, which gives $\tilde{I}_0 = \tilde{I}_1 + \tilde{I}_4 + \tilde{I}_2$ with $\tilde{I}_2 = \tilde{I}_3 + \tilde{I}_5$, where $\tilde{I}_1$ to $\tilde{I}_5$ are the currents flowing through the corresponding impedance/resistors. We simplify this network circuit to an equivalent linear circuit that is easier to analyze (Figure 6b). In Figure 6b, R_{3s}, R_{4s} and R_{5s} represent the equivalent total resistances of the current path prior to R_3, R_4, and R_5 respectively, while other components are identical to those shown in Figure 6a. The total impedance of this circuit is,

$$Z_{\mathrm{tot}}^{*}=\frac{\widetilde{U}_0}{\tilde{I}_0}=\frac{1}{\frac{1}{Z_1^{*}}+\frac{1}{R_{4s}+R_4}+\frac{1}{\frac{(R_{5s}+R_5)(R_{3s}+R_3)}{(R_{5s}+R_5)+(R_{3s}+R_3)}+Z_2^{*}}}=\frac{1}{\frac{1}{Z_1^{*}}+a+\frac{1}{b+Z_2^{*}}}, \tag{14}$$

where $\tilde{U}_0$ is the total voltage between C+ and C- and a and b are real number constants as resistances R_{3s}, R_{3s}, R_{4s}, R_4, R_{5s} and R_5 do not change. According to the voltage divider rule,

$$\frac{\Delta\widetilde{U}}{\widetilde{U}_0}=\frac{R_3}{(R_{3s}+R_3)}\frac{b}{b+Z_2^{*}}=c\frac{b}{b+Z_2^{*}}, \tag{15}$$

where c is again a real number constant representing a constant resistance term. Combining Eq. (2), Eq. (14) and (15) gives,

$$\left|Z_{\mathrm{app}}^{*}\right|e^{\varphi_{\mathrm{app}}i}=\frac{\Delta\widetilde{U}}{\tilde{I}_0}=\frac{bc}{\frac{b+Z_2^{*}}{Z_1^{*}}+aZ_2^{*}+ab+1}. \tag{16}$$

Considering that the intrinsic phase shifts of the earth materials are small negative values ($-0.2 < \varphi < 0$), $\cos\varphi \approx 1$ and $\varphi \approx \sin(\varphi) \approx \tan(\varphi) \approx \tan^{-1}(\varphi)$. Any impedance term Z^* can then be written in rectangular form as $Z^* = |Z^*|\cos(\varphi) + i|Z^*|\sin(\varphi) \approx |Z^*| + i|Z^*|\varphi$. When Z_1^* (located in the positive sensitivity zone of the array) is polarizable (i.e., $\varphi_1 < 0$) and Z_2^* (located in the negative sensitivity zone) is non-polarizable (i.e., $\varphi_2 = 0$), Eq. (16) gives,

$$\varphi_{\text{app}} \approx \varphi_1 \frac{b + |Z_2^*|}{b + |Z_2^*| + a|Z_1^*||Z_2^*| + ab|Z_1^*| + |Z_1^*|}, \tag{17}$$

which explicitly shows that $\varphi_{\text{app}} < 0$, being a measurement signal with normal polarity. On the contrary, if Z_2^* is polarizable (i.e., $\varphi_2 < 0$) and Z_1^* is non-polarizable (i.e., $\varphi_1 = 0$), Eq. (16) results in,

$$\varphi_{\text{app}} \approx -\varphi_2 \frac{|Z_2^*| + a|Z_1^*||Z_2^*|}{b + |Z_2^*| + a|Z_1^*||Z_2^*| + ab|Z_1^*| + |Z_1^*|}, \tag{18}$$

which gives $\varphi_{\text{app}} > 0$, being a measurement signal with negative IP polarity. It can be concluded that the negative IP signals originate from the fact that the impedance is determined from dividing the recorded voltage $\Delta\tilde{U}$ by the input current $\tilde{I}_0$ instead of by the current flowing through the impedance across which $\Delta\tilde{U}$ is recorded, i.e., $\tilde{I}_3$ in our case. It is the phase difference between $\tilde{I}_3$ and measured $\tilde{I}_0$ that gives the non-physical impression of the current lagging the voltage as implied by a positive phase. The circuit model analogy also explains the impact of sensitivity on the resistivity measurements (i.e., resistance measurement in the circuit model). Considering Z_1^* and Z_2^* as pure resistors (i.e., zero phase), Eq. (16) shows that $|Z_{\text{app}}^*|$ increases with the increase of $|Z_1^*|$, whereas it decreases with the increase of $|Z_2^*|$.

5. Frequency dependence

The influence of resistivity and phase variability on the polarity of φ_{app} also has important, hitherto unrecognized, implications for the interpretation of spectral IP datasets. The φ_{app} polarity can vary with frequency if the resistivity of polarizable features changes significantly with frequency, e.g., as observed for electronically conducting materials (e.g., Pelton *et al.* 1978; Wong

1979). We examine this effect using the same synthetic model structure shown in Figure 4a but assigning various values of frequency independent $|\rho^*_{\mathrm{bgk}}|$, φ_{bgk} and frequency-dependent $|\rho^*_{\mathrm{block}}|$ and φ_{block}. We define the frequency dependence of the polarizability of the block using a Cole-Cole type model (Cole & Cole 1941; Pelton *et al.* 1978) with parameters previously found to fit laboratory experimental data obtained on a zero valent iron-sand mixture (50% iron by volume) (Slater *et al.* 2005) (Figure 7a). The spectra cover frequencies from 10^{-3} to 10^{4} Hz, with $|\rho^*_{\mathrm{block}}|$ decreasing from 41 to 14 Ω m (from low to high frequency). The φ_{block} ranges from –21 mrad to –174 mrad, with the peak occurring at ~1 Hz. The frequency independent background half-space was assigned $\varphi_{\mathrm{bgk}} = -1$ mrad, with the $|\rho^*_{\mathrm{bgk}}|$ set to either 10, 30 or 55 Ω m in order to simulate scenarios with $|\rho^*_{\mathrm{bgk}}|$ lower, close to or higher than $|\rho^*_{\mathrm{block}}|$ (Figure 7a).

Figure 7b shows the apparent parameters $|\rho^*_{\mathrm{app}}|$ and φ_{app} from the single measurement for a dipole-dipole array (E10=C+, E12=C-, E14=P-, E16=P+) at various frequencies. Three simulations result in completely different shapes of φ_{app} curves when only the resistivity contrast between the target and the background changes between the simulations. For the highest background resistivity, $|\rho^*_{\mathrm{bgk}}| = 55$ Ω m, the φ_{app} spectra are negative and display a negative peak similar to the φ_{block} spectrum. When $|\rho^*_{\mathrm{bgk}}|$ is reduced to 30 Ω m, φ_{app} is negative at high frequencies but increases to be positive below around 20 Hz. Peaks are observed in both positive and negative apparent phase domains. For the lowest background resistivity $|\rho^*_{\mathrm{bgk}}| = 10$ Ω m, all φ_{app} values become positive and a peak of φ_{app} toward more positive values is observed.

The differences among the three φ_{app} curves can be explained by the difference in resistivity of $|\rho^*_{\mathrm{block}}|$ relative to $|\rho^*_{\mathrm{bgk}}|$ and how this difference affects the sensitivity distribution, as demonstrated in Section 3.2. Positive φ_{app} values are found when $|\rho^*_{\mathrm{block}}|/|\rho^*_{\mathrm{bgk}}|$ is relatively high, being the case when $|\rho^*_{\mathrm{bgk}}| = 10\ \Omega$ m for all frequencies and when $|\rho^*_{\mathrm{bgk}}| = 30\ \Omega$ m at low frequencies. The $|\rho^*_{\mathrm{app}}|$ spectra also differ between the three simulations, exhibiting a frequency dependence consistent with the polarity of φ_{app}. The percentage frequency effect (PFE = ($|\rho^*_{\mathrm{app}}|_{\mathrm{L}} - |\rho^*_{\mathrm{app}}|_{\mathrm{H}}$) / $|\rho^*_{\mathrm{app}}|_{\mathrm{L}}$, where subscripts $_{\mathrm{H}}$ and $_{\mathrm{L}}$ refer to a high and low measurement frequency, respectively) is another measure of the IP effect that was popular in mineral exploration (Ward 1988). Figure 7b shows that a negative PFE (i.e., increasing $|\rho^*_{\mathrm{app}}|$ with increasing frequencies) is always observed when φ_{app} is positive. Just as with positive φ_{app} values, a negative PFE is non-physical from the perspective of IP mechanisms and another representation of negative IP effects in frequency domain IP measurements.

In summary, this simulation of frequency dependent data demonstrates the possibility of a wide range of φ_{app} spectra, which can be very different from the spectra of an intrinsic polarizable target. This has significant implications with respect to the interpretation of field-measured phase curves.

6. Sandbox experiments

Laboratory sandbox experiments were conducted to verify the observations from numerical modeling (Figure 8a). A sandbox 36 cm wide, 15 cm high and 55 cm long was filled with sand fully saturated with tap water (resistivity of 40 Ω m at 25 °C). Four electrodes were deployed in the central area of the sandbox with a 5 cm spacing. The distance between the electrodes and the box wall was large enough to ignore boundary effects on the measurements. FDIP (from 0.1 to 100 Hz) and TDIP data (1 Hz waveform) were measured using an Ontash & Ermac PSIP instrument and an IRIS Syscal Pro instrument, respectively. φ_{app} and M_{app} of the background sand was –2 mrad and 2 mV/V respectively, providing a low polarizability background matrix.

To simulate a scenario similar to the synthetic model in Section 5, a piece of the iron mineral magnetite (dimensions approximately 8 cm length, 4 cm height and 5 cm width) was buried between the middle two electrodes at 2 cm depth. The φ_{app} collected using the dipole-dipole array is negative at high frequencies and then increases to positive values below 4 Hz (Figure 8b). The spectral shape of φ_{app} in Figure 8b is similar to the shape of the 0.1-200 Hz segment of the simulated blue φ_{app} curve ($|\rho^*_{bgk}| = 30\ \Omega$ m) in Figure 7b. The M_{app} measured with the dipole-dipole array is –42.5 mV/V, also indicating a negative IP response. Its polarity is consistent with the φ_{app} polarity at low frequencies. For the Wenner array measurement, a conventional negative φ_{app} spectrum is observed (Figure 8c) as the polarizable magnetite falls within the positive sensitivity zones of this array (Figure 2b). The M_{app} measured by the Wenner array is positive (27.8 mV/V), being consistent with the negative φ_{app} recorded in the frequency domain. These laboratory experiments therefore confirm the observations from numerical modeling and theory.

7. Conclusions

In a heterogenous polarizable subsurface the apparent phase φ_{app} recorded in surface four-electrode FDIP measurements may be positive. The polarity of φ_{app} is associated with the sensitivity distribution of a four-electrode measurement layout and is determined by the intrinsic phase and resistivity of the subsurface. Considerations of the sensitivity patterns of complex resistivity measurements theoretically confirm the occurrence of positive φ_{app}, i.e., for a non-polarizable subsurface, placing a small, highly polarizable object in the negative and positive sensitivity zones will result in positive and negative φ_{app}, respectively. This is consistent with a simplified electric circuit model, which physically explains the negative IP (i.e., the paradox of current appearing to lag voltage) to result from the measured voltage drop across the potential electrodes being divided by the input current at the current electrodes instead of the current flowing through the impedance across the potential electrodes.

Numerical modeling shows the φ_{app} polarity is dictated by the relative values of both the intrinsic phase and the intrinsic resistivity of a polarizable heterogeneity compared to the background medium. The control of the relative strength of the intrinsic resistivity on φ_{app} results from its influence on the sensitivity distribution of a measurement. In the case that the intrinsic resistivity varies significantly with frequency, the φ_{app} polarity can vary with frequency in FDIP measurements, which results in φ_{app} spectra that are very different from the intrinsic phase spectrum. This finding is confirmed by laboratory sandbox experiments where φ_{app} of a dipole-dipole array on a buried piece of magnetite is negative from 100 to 4 Hz and then becomes positive below 4 Hz. Our results emphasize the need to accurately quantify error sources in FDIP measurements as positive φ_{app} measurements should be expected, are likely to be common in heterogeneous systems and should not simply be discarded prior to further data processing e.g. inversion. This observation is consistent with previously studied negative apparent chargeability data in TDIP measurements.

Acknowledgements

This research was partly funded by the U.S. Department of Energy under grant DE-SC0016412 and a Rutgers University-Newark Graduate School Dissertation Fellowship award to C. Wang.

Supplemental funding for this project was provided by the Rutgers University-Newark Chancellor's Research Office. C. Wang thanks Sina Saneiyan (Rutgers University-Newark) for guidance on the use of ResIPy. We thank Andreas Hördt, Konstantin Titov, Timothy Johnson and an anonymous reviewer for their valuable comments that improved the quality of the paper.

Data availability

The data from this work is available upon request from the corresponding author.

References

Abdulsamad, F., Florsch, N., Schmutz, M. & Camerlynck, C. (2016) Assessing the high frequency behavior of non-polarizable electrodes for spectral induced polarization measurements. *J. Appl. Geophys.*, **135**, 449–455, Elsevier B.V. doi:10.1016/j.jappgeo.2016.01.001

Bate, B., Cao, J., Zhang, C. & Hao, N. (2020) Spectral induced polarization study on enzyme induced carbonate precipitations: influences of size and content on stiffness of a fine sand. *Acta Geotech.*, **8**, Springer Berlin Heidelberg. doi:10.1007/s11440-020-01059-8

Binley, A. (2015) *Tools and Techniques: Electrical Methods*. *Treatise Geophys. Second Ed.*, Vol. 11, Elsevier B.V. doi:10.1016/B978-0-444-53802-4.00192-5

Binley, Andrew & Kemna, A. (2005) DC resistivity and induced polarization methods. in *Hydrogeophysics* eds. Rubin, Y. & Hubbard, S.S., pp. 129–156, Springer.

Blanchy, G., Saneiyan, S., Boyd, J., McLachlan, P. & Binley, A. (2020) ResIPy, an intuitive open source software for complex geoelectrical inversion/modeling. *Comput. Geosci.*, **137**, 104423, Elsevier Ltd. doi:10.1016/j.cageo.2020.104423

Cole, K. s. & Cole, R.H. (1941) Dispersion and Absorption in Dielectrics I. Alternating Current Characteristics. *J. Chem. Phys.*, **9**, 341–351.

Dahlin, T. & Loke, M.H. (2015) Negative apparent chargeability in time-domain induced polarisation data. *J. Appl. Geophys.*, **123**, 322–332, Elsevier B.V. doi:10.1016/j.jappgeo.2015.08.012

Flores, A., Kemna, A., Oberdörster, C., Zschornack, L., Leven, C., Dietrich, P. & Weiss, H. (2012) Delineation of subsurface hydrocarbon contamination at a former hydrogenation plant using spectral induced polarization imaging. *J. Contam. Hydrol.*, **136–137**, 131–144, Elsevier B.V. doi:10.1016/j.jconhyd.2012.06.001

Flores Orozco, A., Bücker, M., Steiner, M. & Malet, J.P. (2018) Complex-conductivity imaging for the understanding of landslide architecture. *Eng. Geol.*, **243**, 241–252, Elsevier. doi:10.1016/j.enggeo.2018.07.009

Garcia-Artigas, R., Himi, M., Revil, A., Urruela, A., Lovera, R., Sendrós, A., Casas, A., *et al.* (2020) Time-domain induced polarization as a tool to image clogging in treatment wetlands. *Sci. Total Environ.*, **724**. doi:10.1016/j.scitotenv.2020.138189

Kelter, M., Huisman, J.A., Zimmermann, E. & Vereecken, H. (2018) Field evaluation of broadband spectral electrical imaging for soil and aquifer characterization. *J. Appl. Geophys.*, **159**, 484–496, Elsevier B.V. doi:10.1016/j.jappgeo.2018.09.029

Kemna, A. (2000) *Tomographic inversion of complex resistivity – Theory and application*, PhD thesis, Ruhr-University of Bochum.

Komarov, V. (1960) Bases of application of the induced polarization method for prospecting of ore deposits. *Methodol. Tech. Explor.*, **23**, 7–17.

Komarov, V. (1980) *Electrical prospecting with Induced Polarization method*, Leningrad: Nedra Press.

Lesmes, P. & Frye, M. (2001) Influence of pore fluid chemistry on the complex conductivity and induced polarization responses of Berea sandstone. *J. Geophys. Res.*, **106**, 4079–4090.

Liu, W., Chen, R., Cai, H., Luo, W. & Revil, A. (2017) Correlation analysis for spread-spectrum induced-polarization signal processing in electromagnetically noisy environments. *Geophysics*, **82**, E243–E256. doi:10.1190/GEO2016-0109.1

Luo, Y. & Zhang, G. (1998) 2. Forward Theory of Spectral Induced Polarization. in *Theory and Application of Spectral Induced Polarization*, pp. 13–90, Society of Exploration Geophysicists. doi:10.1190/1.9781560801856.ch2

Mary, B., Saracco, G., Peyras, L., Vennetier, M., Mériaux, P. & Camerlynck, C. (2016) Mapping tree root system in dikes using induced polarization: Focus on the influence of soil water content. *J. Appl. Geophys.*, **135**, 387–396, Elsevier B.V. doi:10.1016/j.jappgeo.2016.05.005

Nabighian, M.N. & Elliot, C.L. (1976) NEGATIVE INDUCED-POLARIZATION EFFECTS FROM LAYERED MEDIA. *GEOPHYSICS*, **41**, 1236–1255. doi:10.1190/1.2035915

Ntarlagiannis, D., Robinson, J., Soupios, P. & Slater, L. (2016) Field-scale electrical geophysics over an olive oil mill waste deposition site: Evaluating the information content of resistivity versus induced polarization (IP) images for delineating the spatial extent of organic contamination. *J. Appl. Geophys.*, **135**, 418–426, Elsevier B.V. doi:10.1016/j.jappgeo.2016.01.017

Pelton, W.H., Wards, S.H., Hallof, P.G., Sill, W.R. & Nelson, P.H. (1978) Mineral Discrimination and Removal of Inductive Coupling with Multifrequency IP. *Geophyics*, **43**, 588–609.

Saneiyan, S., Ntarlagiannis, D., Ohan, J., Lee, J., Colwell, F. & Burns, S. (2019) Induced polarization as a monitoring tool for in-situ microbial induced carbonate precipitation (MICP) processes. *Ecol. Eng.*, **127**, 36–47, Elsevier. doi:10.1016/j.ecoleng.2018.11.010

Saneiyan, S., Ntarlagiannis, D., Werkema, D.D. & Ustra, A. (2018) Geophysical methods for monitoring soil stabilization processes. *J. Appl. Geophys.*, **148**, 234–244, Elsevier B.V. doi:10.1016/j.jappgeo.2017.12.008

Seigel, H.O. (1959) MATHEMATICAL FORMULATION AND TYPE CURVES FOR INDUCED POLARIZATION. *GEOPHYSICS*, **24**, 547–565. doi:10.1190/1.1438625

Slater, L.D., Choi, J. & Wu, Y. (2005) Electrical properties of iron-sand columns: Implications for induced polarization investigation and performance monitoring of iron-wall barriers. *Geophysics*, **70**, G87. doi:10.1190/1.1990218

Slater, L.D. & Lesmes, D. (2002) IP interpretation in environmental investigations. *Geophysics*, **67**, 77–88. doi:10.1190/1.1451353

Sumner, J.S. (1976) *Principles of induced polarization for geophysical exploration*, Elsevier.

Voorhis, G.D. Van, Nelson, P.H. & Drake, T.L. (1973) COMPLEX RESISTIVITY SPECTRA OF PORPHYRY COPPER MINERALIZATION. *GEOPHYSICS*, **38**, 49–60. doi:10.1190/1.1440333

Ward, S.H. (1988) The Resistivity and Induced Polarization Methods. *Symp. Appl. Geophys. to Eng. Environ. Probl. 1988*, pp. 109–250, Environment and Engineering Geophysical Society. doi:10.4133/1.2921804

Wong, J. (1979) An electrochemical model of the induced-polarization phenomenon in disseminated sulfide ores. *GEOPHYSICS*, **44**, 1245–1265. doi:10.1190/1.1441005

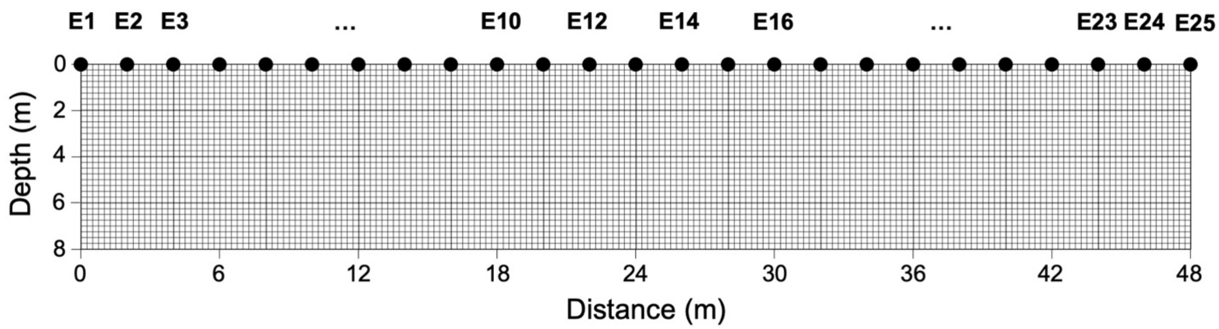

Figure 1. Numerical modeling set up with 25 electrodes (E1 to E25) on a model space using 0.25 × 0.25 m mesh cells.

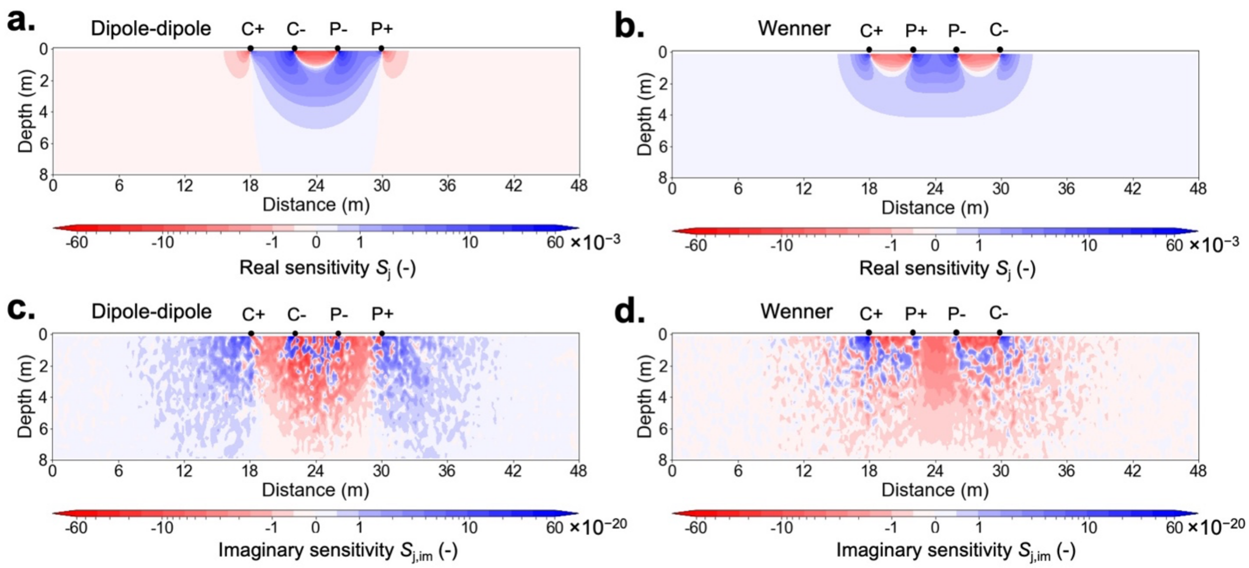

Figure 2. Sensitivity distribution of complex resistivity measurements using electrodes E10, E12, E14 and E16 for a 100 Ω m and –1 mrad homogeneous half space. (a) Real sensitivity of dipole-dipole array (E10=C+, E12=C-, E14=P-, E16=P+). (b) Real sensitivity of Wenner array (E10=C+, E12=P+, E14=P-, E16=C-). (c) Imaginary sensitivity of dipole-dipole array. (d) Imaginary sensitivity of Wenner array.

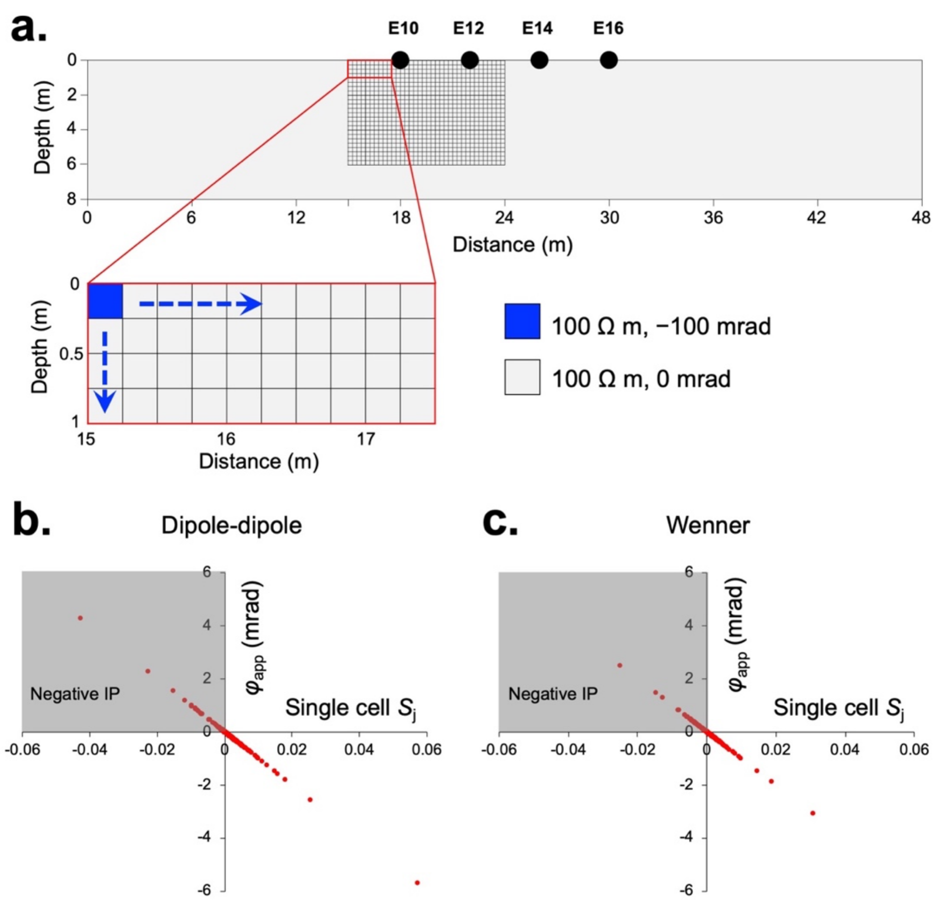

Figure 3. Numerical modeling of the influence of sensitivity polarity on the φ_{app} polarity. (a). Illustration of the model configuration; a polarizable cell (blue) moves to the right and down one cell by one cell (in the zoomed in figure) to cover the region of 15 to 24 m distance and 0 to 6 m depth (meshed region in the zoomed out figure); with the polarizable cell in each location, φ_{app} for a dipole-dipole array (E10=C+, E12=C-, E14=P-, E16=P+) and a Wenner array (E10=C+, E12=P+, E14=P-, E16=C-) were computed; (b) and (c). φ_{app} for a dipole-dipole (b) and Wenner (c) array versus the sensitivity S_j (unitless) of the single cell containing the polarizable cell (blue cell in 3a); Grey shaded quadrants highlight the negative IP responses.

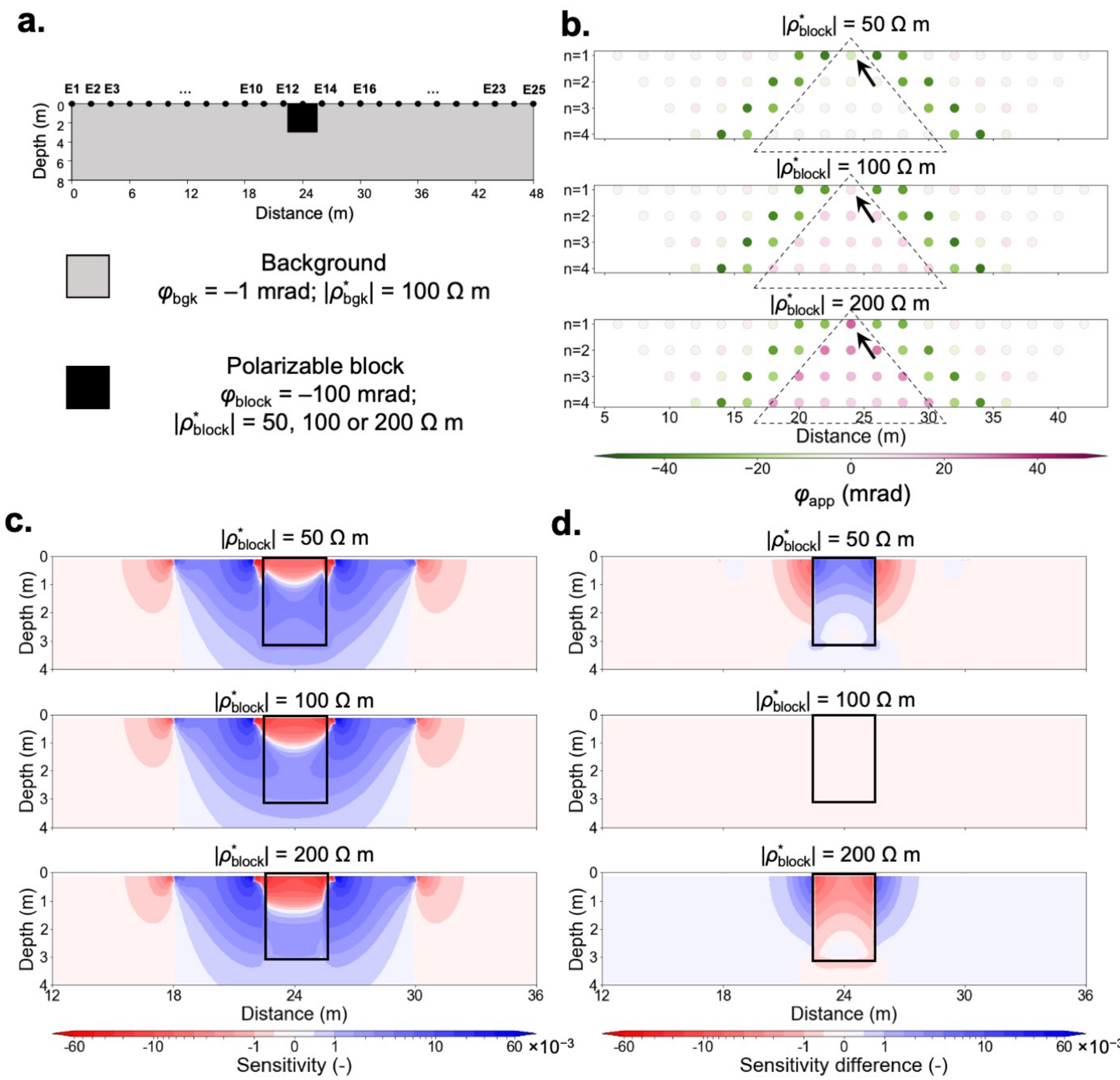

Figure 4. Influence of resistivity heterogeneity on the φ_{app} polarity. (a). Synthetic model settings. (b). Pseudosection of φ_{app} at various values of $|\rho^*_{\text{block}}|$ ($|\rho^*_{\text{block}}|$ =100 Ω m is the homogeneous resistivity condition); data within the dashed triangles are influenced by $|\rho^*_{\text{block}}|$. (c). Sensitivity distribution of the single four-electrode measurement pointed out by the arrow in (b) with various $|\rho^*_{\text{block}}|$ corresponding to the pseudosections. (d). Sensitivity difference relative to that of $|\rho^*_{\text{block}}|$ =100 Ω m.

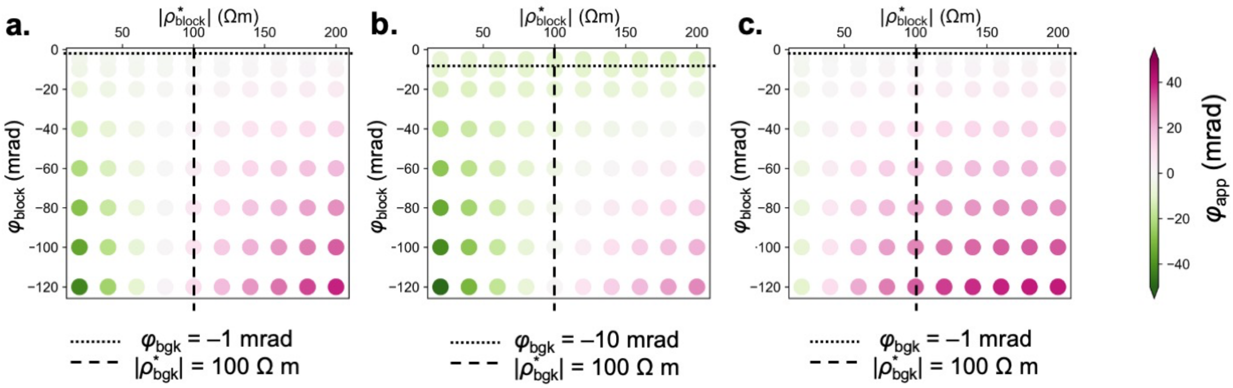

Figure 5. Impacts of $|\rho^*_{block}|$ and φ_{block} on the modeled φ_{app} under various conditions. (a) and (b). φ_{app} modeled using a dipole-dipole array (E10=C+, E12=C-, E14=P-, E16=P+) for the synthetic structure shown in Figure 4a under various background settings (indicated by dotted and dashed lines). (c). φ_{app} modeled with the same settings as (a) but with vertical extent of polarizable block in Figure 4a reduced to be between 0 and 1 m.

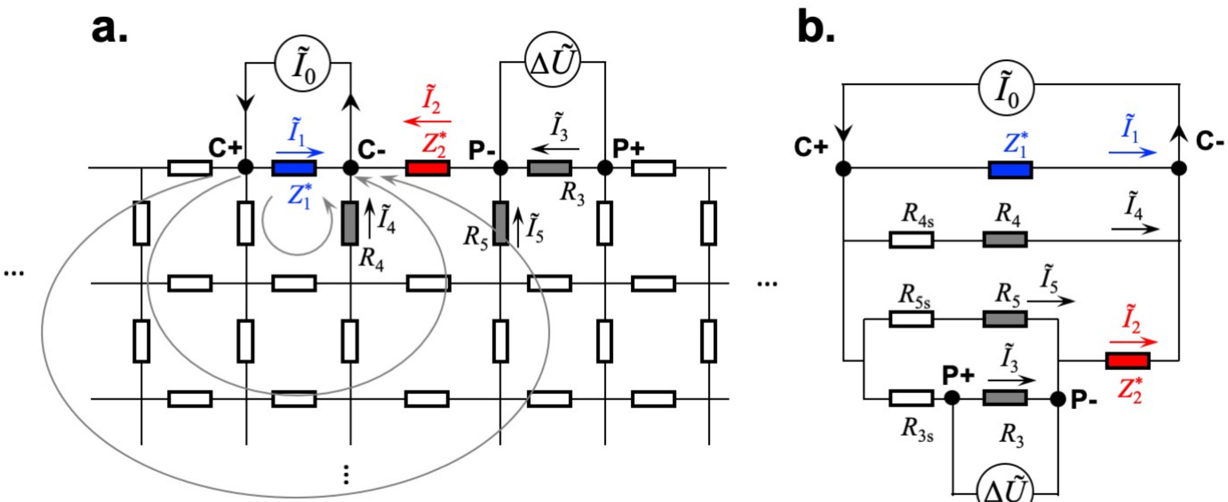

Figure 6. (a). Electrical conduction through the subsurface modeled as a resistor/impedance network circuit; grey arrows illustrate idealized current flow directions in a real subsurface space for comparison; (b) A simplified equivalent linear electrical circuit of the circuit conceptualized in (a).

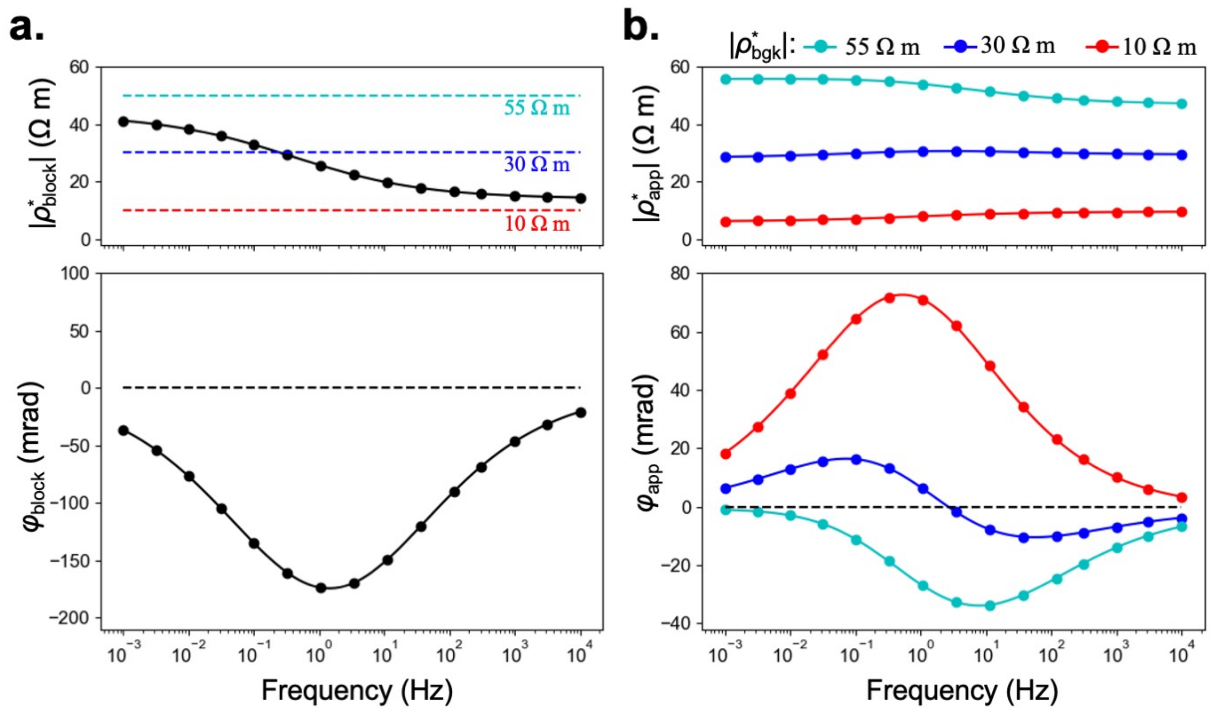

Figure 7. Simulation based on a polarizable block with frequency-dependent complex resistivity using model structure shown in Figure 4a (a). Intrinsic resistivity and phase spectra of the polarizable block and the selection of frequency-independent background resistivity (colored dashed lines); black dashed line represents φ_{block} = 0 mrad; (b). $|\rho^*_{app}|$ and φ_{app} spectra under different $|\rho^*_{bgk}|$ conditions; black dashed line represents φ_{app} = 0 mrad.

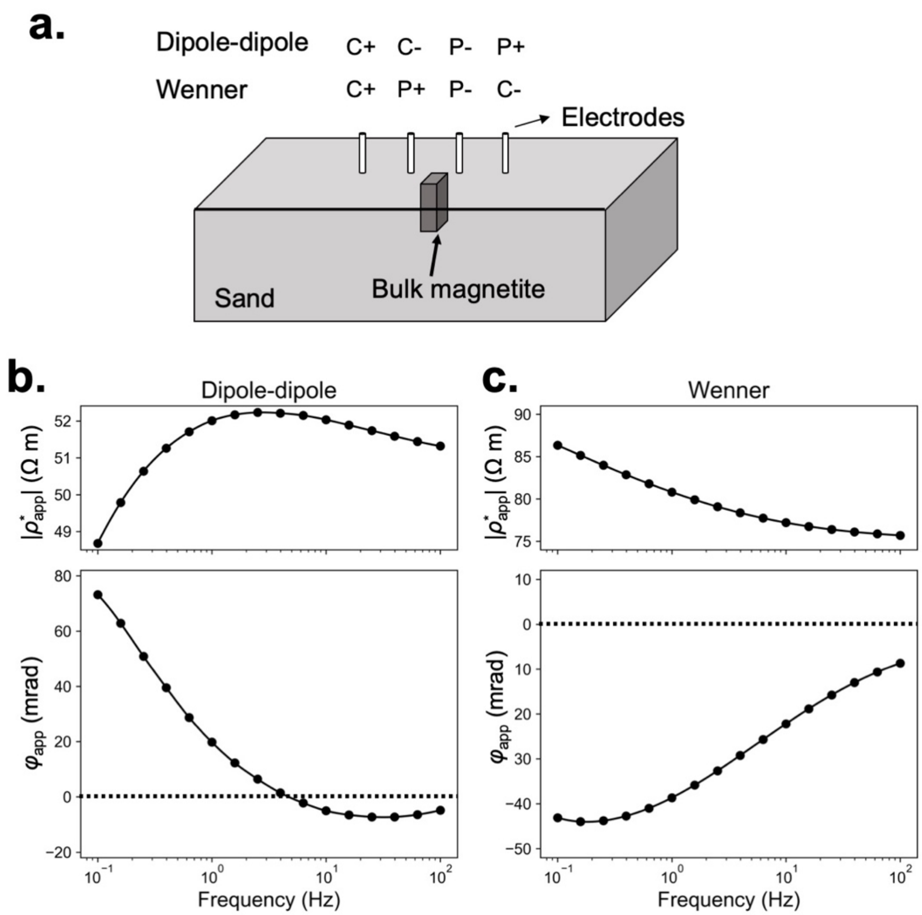

Figure 8. Sandbox experiments. (a) Schematic diagram of sandbox experimental set-up. (b). $|\rho^*_{app}|$ and φ_{app} spectra measured by dipole-dipole array; black dashed line represents φ_{app} = 0 mrad (c) $|\rho^*_{app}|$ and φ_{app} spectra measured by Wenner array; black dashed line represents φ_{app} = 0 mrad.